Water Air Soil Pollut (2024) 235:208
https://doi.org/10.1007/s11270-024-07015-6

Preparation of Nickel Slag–Based Microelectrolysis Filler Material and Eco-friendly Utilization in the Degradation of Azo Compound Wastewater

Jiaxing Cai · Yue Zhang · Yunye Cao

Received: 23 November 2023 / Accepted: 28 February 2024 / Published online: 12 March 2024

Abstract A microelectrolytic filler (MEF) was prepared on the based on the concept of "treating waste with waste," using nickel slag as raw material through the carbon thermal reduction method. The degradation rate of methyl orange (MO) in water was used to evaluate the performance of the MEF. The effects of the preparation conditions and reaction parameters on the MEFs were investigated. The results showed that the degradation rate of MO was the highest when the dosage of coal was 35%, the roasting time was 80 min, the dosage of MEF was 7 g/L, and the initial pH of the solution was 2. The MEF was applied on degradation of azo compound in wastewater. Under the best conditions, the degradation rate of MO reached on 99.66% at 5 min, and it was nearly completely degraded at 60 min. The X-ray powder diffractometer (XRD) and scanning electron microscopy (SEM) analysis results indicated that iron oxides from nickel slag were reduced to zero-valent iron (ZVI) as MEF with the temperature increasing. The degradation mechanism was analyzed by ultraviolet (UV) absorption spectroscopy and density functional theory (DFT) study. The results showed that the degradation of MO in water was due to the destruction of the azo double bond of MO by the active hydrogen [H] produced in the microelectrolytic system. MO was degraded to produce the intermediate sulfanilic acid (SA), which continued to degrade. DFT calculations showed that the adsorption of surfaces and citric acid and its degradation products on Fe surfaces was mainly attributed to the Fe–O chemical bonding between the Fe atoms in the substrate surface and the oxygen atoms in the molecule.

Keywords Nickel slag · Microelectrolytic filler · Azo compound · DFT

J. Cai · Y. Cao (✉)
School of Materials Science and Chemical Engineering, Ningbo University, Ningbo, Zhejiang 315211, China
e-mail: caoyunye@nbu.edu.cn

J. Cai
e-mail: caijiaxing0228@163.com

Y. Zhang
Department of Civil Engineering, Qingdao University of Technology, Qingdao, China
e-mail: zhangyue1723@gmail.com

Y. Cao
State Key Laboratory of Mineral Processing, Beijing 102628, China

Y. Cao
State Key Laboratory of Complex Nonferrous Metal Resources Clean Utilization, Kunming 650093, China

1 Introduction

Nickel slag (NS) is a solid waste produced by high-temperature melt quenching in the process of pyrometallurgy and contains a large amount of iron and some heavy metals, such as nickel, copper, and cobalt (Peng et al., 2018). With the mining of nickel–iron alloys

around the world, NS has gradually become one of the main solid wastes. However, the secondary utilization rate of NS is only 8% (Sun et al., 2023). If not properly utilized, it can cause significant harm to the environment. Currently, NS is primarily used in building materials. Zaharak (Zaharaki & Komnitsas, 2009) added NS to cement mortar to improve its strength in the later stages. Maragko (Maragkos et al., 2009) used NS to produce a compact cementing material with low water absorption and a compressive strength of 118 MPa. However, the application of NS in wastewater treatment is rarely studied. Wu (Wu et al., 2022) utilized NS as a raw material and synthesized zeolite through hydrothermal synthesis, modified it, and used it as an adsorbent for phosphorus. Additionally, there have been studies conducted on NS for wastewater treatment.

With the rapid development of various industries, it also produces a large amount of wastewater, which seriously threatens the safety and health of human beings. For treatment of wastewater pollution problem, researchers had reduced pollution through different techniques such as biological treatment (Arsalan et al., 2020; Arsalan and Sarrafzadeh, 2018, Arsalan and Sarrafzadeh, 2019), single atomic site catalytic treatment (Ge et al., 2021, 2023, 2024), and advanced oxidation treatment (Emad and Chaudhuri, 2009; Sood et al., 2016). Azo dyes are common pollutants which are stable and difficult to degrade due to their chemical structure as aromatic compounds with one or more azo groups (Yang et al., 2010). Therefore, there is a need for a low-cost and efficient method to control it. At present, iron-carbon microelectrolysis technology has been proved to treat various kinds of wastewater, such as chemical wastewater (Sun et al., 2013), pharmaceutical wastewater (Yu et al., 2019a, b), dye wastewater (Wang et al., 2018), and others (Zhu et al., 2014). The iron-carbon electrode system can be expressed as follows:

Anode:

$$Fe^{2+}(aq) + 2e^{-} \rightleftharpoons Fe(s)\ \varphi^{\theta}\left(Fe^{2+}/Fe\right) = -0.44V \quad (1)$$

Cathode:

$$2H^{+}(aq) + 2e^{-} \rightleftharpoons H_2(g)\ \varphi^{\theta}\left(H^{+}/H_2\right) = 0V \quad (2)$$

In the abovementioned reactions, the active hydrogen [H] produced by the cathode exhibits strong chemical activity, which can effectively break down the carbon chain in the pollutant until it is completely degraded into CO_2, H_2O, and small molecules (Gomathi Devi et al., 2009).

Currently, various environmental pollutants can be degraded through different methods, but the degradation mechanism is not fully understood. Previous studies have mainly relied on speculation based on products observed after degradation, and detecting the intermediates produced during the degradation process has been challenging. More and more researchers are using quantum chemistry to study the reaction mechanism (Liu et al., 2018; Zhang et al., 2007, 2014). Theoretical calculations (Dai et al., 2016; Sun et al., 2020) can help fully comprehend the degradation process of organic pollutants and compensate for the limitations of the experimental approaches. Therefore, density functional theory (DFT) can better reveal the complex degradation process of organic pollutants.

In previous studies, iron sources used to prepare microelectrolytic filler (MEF) usually involved direct utilization of zero-valent iron (ZVI) (Ma et al., 2023; Zhou et al., 2013a, b) or iron salt (Wang et al., 2017a, b) through solution reactions. However, few people were able to produce MEF from waste. Using waste to produce MEF could not only reduce costs, but also solve some environmental problems. In this study, an MEF was prepared based on the basis of the concept of "treating waste with waste" by using waste NS and coal through a carbothermal reduction process, with methyl orange (MO) serving as a simulated pollutant. The performance of the MEF was evaluated based on the degradation rate of MO. The study also examined the effects of preparation conditions and reaction parameters on the degradation of pollutants. The mechanism of MO degradation was described using ultraviolet (UV) absorption spectroscopy and DFT study.

2 Materials Characteristics and Study Methods

2.1 Raw Materials

In this study, nickel slag was used as iron source and coal as reducing agent. Both nickel slag and coal

were obtained from a resource company in Beijing. The nickel slag was 35.01% iron and 2.19% nickel. The composition of coal was as follows: moisture 2.92%, fixed carbon 79.19%, ash 10.62%, and volatile 7.27%. Nickel slag and coal were crushed to a size of ≤ 0.1 mm for use. Methyl Orange (average Mw ~ 327.33) was from Macklin. Anhydrous sodium carbonate (average Mw ~ 105.99) was from Macklin (Shanghai, China). All water used is deionized.

2.2 Preparation Process of MEF

NS (20 g) was thoroughly mixed with coal (25–45%) and 0.6 g sodium carbonate and then placed into a clay–graphite crucible. One gram of coal was covered on the surface of the sample and the crucible was covered with a cap to maintain a reducing atmosphere. The samples were then roasted in a muffle furnace. Once the specific temperature was reached, the clay–graphite crucible containing the sample was quickly placed into the muffle furnace for roasting. After roasting, the sample was cooled in air to room temperature. Once cooled, the coal covering the surface was removed. The sample was crushed to less than 0.1 mm for subsequent use.

2.3 Experimental Steps

The effects of coal dosage, roasting time, MEF dosage, and initial solution pH on MO degradation by MEF were studied. The sample was put into a beaker containing MO solution with an initial concentration of 100 mg/L for the experiment. The initial pH value of the solution was adjusted using sulfuric acid and sodium hydroxide and measured with a digital pH meter (pH 848, China). Furthermore, all reactions were conducted in a water bath at 25 °C to reduce the influence of water temperature on the reaction. The reaction solution was stirred using a mechanical stirrer (HJ-4S, China) at 350 ± 20 rpm (Fig. 1). After the solution reaction, the water sample was collected through a 0.45-μm filter.

2.4 Analytical Methods and Characterization

The residual concentration of the MO in the solution was determined using an UV–vis spectrophotometer (UV-2501PC, Hitachi, Japan). The detection wavelength of the MO was 464 nm. If necessary, the sample solution could be diluted twice before testing.

The degradation rate of the MO is defined as follows:

$$R = \frac{C_0 - C_t}{C_0} \times 100\% \quad (3)$$

where R is the degradation rate, C_0 is the initial concentration of the MO in the solution, and C_t is the concentration of the MO at time t (min).

To characterize the sample, it was fixed in epoxy resin for scanning electron microscopy (SEM, SU5000, Hitachi, Japan) and energy-dispersive spectrometer (EDS, X Flash 6160, Bruker, Germany) analysis. Phase analysis of the sample was performed by X-ray powder diffractometer (XRD, D8, Bruker,

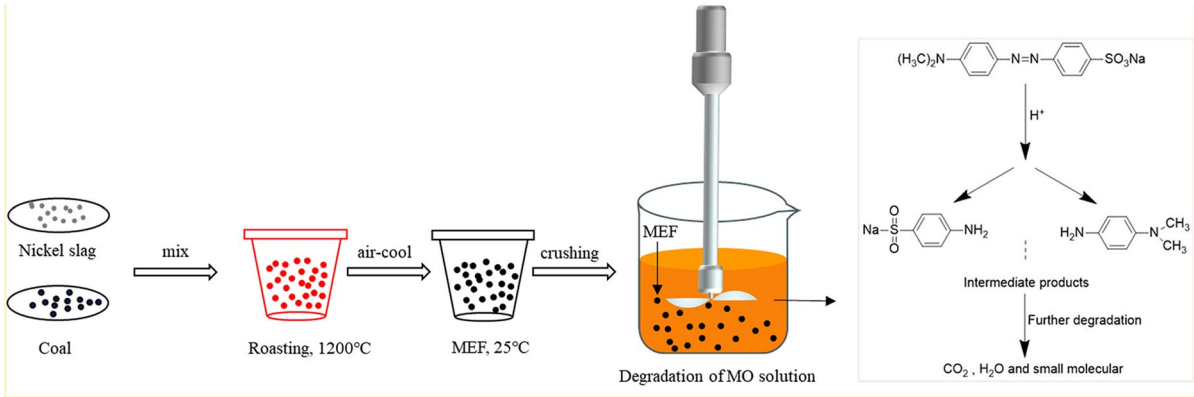

Fig. 1 The experimental details

Germany) under the following conditions: Cu-Kα radiation with a step of 0.02°.

2.5 DFT Calculation Detail

The first-principal calculation was performed using Vienna Ab initio simulation package (VASP) code, employing periodic condition based on a plane-wave basis set. The Perdew, Burke, and Ernzerhof (PBE) exchange correction functionals (Hammer et al., 1999) were chosen because they provided a good match between experimental and DFT calculations in silicate materials. The projector augmented-wave method was used to describe the electronic structure, with a plane wave basis set cutoff energy of 500 eV, which was verified to be sufficient for fully converged energy results. The relaxation of electronic degrees of freedom was stopped when the total energy between two steps was smaller than 1.0×10^{-5} eV. Brillouin zone integration was achieved using the Monkhorst–Pack scheme (Monkhorst & Pack, 1976) with a $1\times1\times1$ k-point sampling for the geometry optimization during the adsorption of methyl orange on Fe (100) surface. The conjugate-gradient algorithm was employed to relax the ions into their instantaneous ground state, with a force convergence tolerance set to 0.02 eV/Å. A semi-empirical dispersion correction method (Grimme's DFT-D3) (Grimme, 2006) was applied in all the three dimensions in calculations. Due to the different top and bottom layers of the slab used to mimic the surface, diploe corrections were applied in the calculation; the dipole moment was calculated parallel to the *z*-direction. The Fe (100) surface slab model had dimensions 9.7 Å×19.4 Å×26 Å, with a 20-Å-thick vacuum layer to prevent chemical interaction with the adjacent image.

3 Results and Discussion

3.1 Characterization

The increase of the roasting time is conducive to the generation of MEF, so it was investigated that the function of roasting time on obtaining ZVI from nickel slag. XRD and SEM–EDS were employed for the characterization of mineral's components of the MEF samples obtained at different roasting time, as shown in Fig. 2.

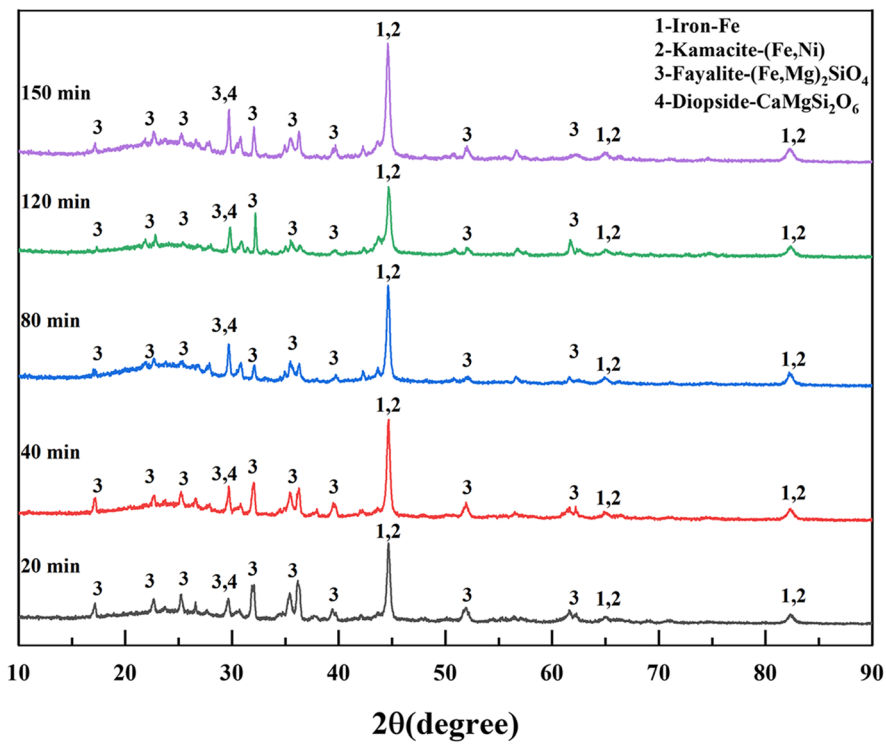

Fig. 2 The XRD patterns of different roasted products on different roasting time at 1200 ℃

The XRD pattern shows that the synthesized samples mainly contain ZVI. With the increase in reaction time, minerals containing iron gradually transform to ZVI, which can form the widely reported Fe–C microelectrolytic system with unreacted residual carbon in the sample (Yu et al., 2016).

Most of the iron sources in NS are hematite (Fe_2O_3), and the reduction process of iron compounds to ZVI is as follows (Li et al., 2009):

$$2Fe_2O_3 + 3C = 4Fe + 3CO_2 \quad (4)$$

$$C + CO_2 = 2CO \quad (5)$$

$$Fe_2O_3 + 3CO = 2Fe + 3CO_2 \quad (6)$$

Figure 3 shows SEM images of roasted materials at different roasting time at 1200 ℃, where ZVI is represented by bright spots and the gray area represents silicate minerals. As shown in Fig. 3 a–e, with the extension of reaction time, the area of the bright spot increases gradually, which indicates that Fe-containing minerals in NS are gradually transformed into ZVI. According to the EDS and element distribution results, an Fe–C microelectrolytic system can be formed between this ZVI and residual carbon.

3.2 Optimization on Preparation Conditions of MEF

The roasting time and coal dosage (Wang et al., 2017a, b) are important factors affecting the reduction

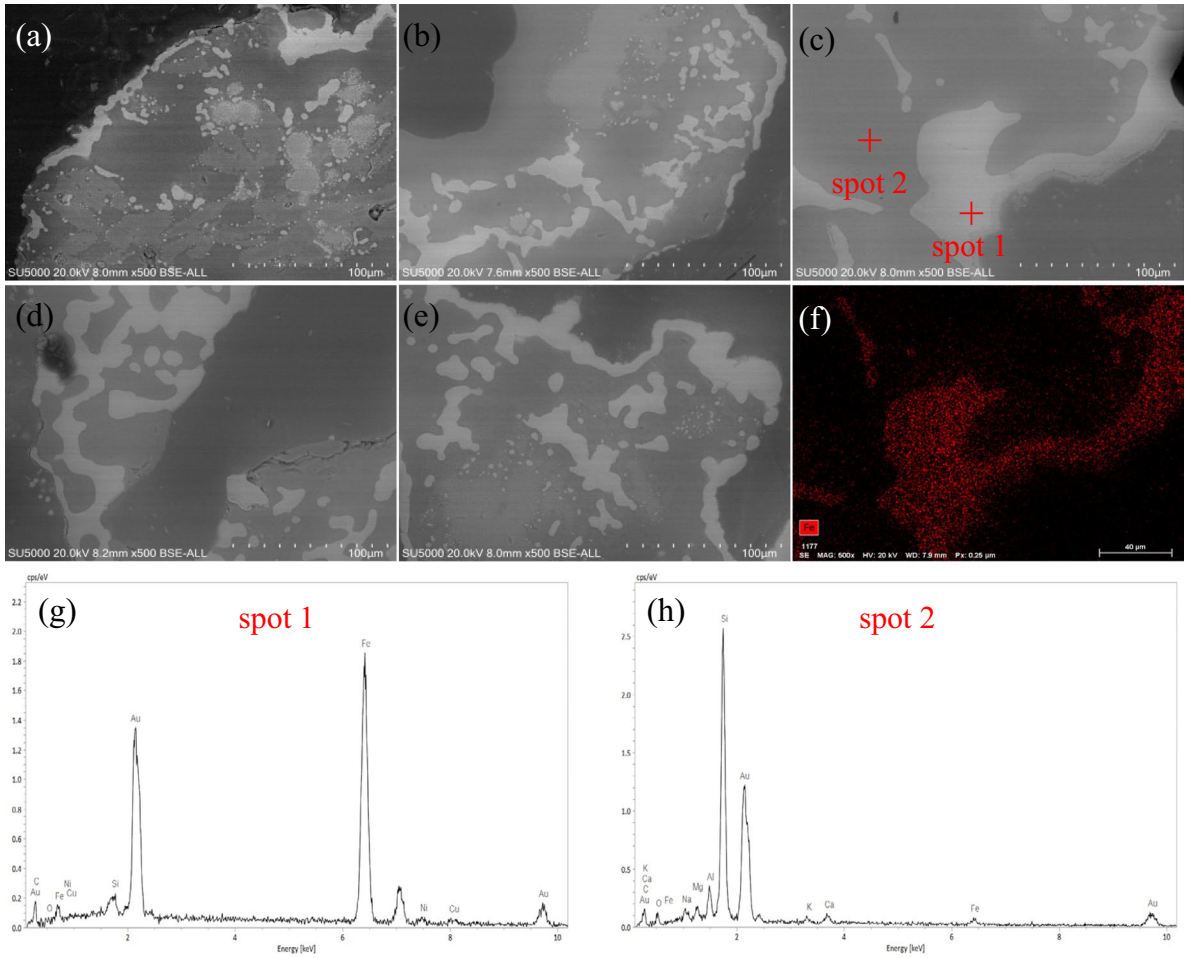

Fig. 3 SEM images of MEF at different roasting time: **a** 20 min, **b** 40 min, **c** 80 min, **d** 120 min, **e** 150 min; **f** distribution of Fe elements in picture **c**; **g** EDS analysis results at spot 1; **h** EDS analysis results at spot 2

of iron from the nickel slag to ZVI; thus, they may also influence the degradation rate of MO.

The effects of roasting time (20, 40, 80, 120, and 150 min) on the degradation rate of MO were investigated while keeping other conditions consistent, i.e., roasting temperature of 1200 ℃, coal dosage of 35%, initial pH = 3, and MEF dosage of 5 g/L. As shown in Fig. 4 a, as the roasting time gradually increases from 20 to 80 min, the degradation rate of MO at 5 min also gradually rises to a maximum value of 87.49%. However, with the further increase in roasting time, the degradation rate of MO at 5 min starts to decrease, and the degradation rate at 60 min also reduces. This may be attributed to the increase in the reduction amount of ZVI with the rise in roasting time, which affects the degradation rate of MO. When the roasting time exceeds 80 min, the degradation rate of MO decreases, possibly due to the tendency of ZVI particles to aggregate and the decrease in the proportion of residual carbon content, leading to the inhibition of the formation of Fe–C microcells (Lu et al., 2020). Therefore, the best roasting time is 80 min.

The effects of the coal dosage (25%, 30%, 35%, 40%, and 45%) on the degradation rate of MO were investigated under consistent conditions. As shown in Fig. 4 b, the degradation rate of MO gradually increases at 5 min as the coal dosage rises from 25 to 35%. At a coal dosage of 35%, the degradation rate reaches a maximum of 87.49% at 5 min and remains at 97.93% at 60 min. This phenomenon may be attributed to the increase in amount of residual carbon in the sample with the rise in coal dosage, thereby improving the number of reaction sites. However, when the coal dosage exceeds 35%, the proportion of Fe–C in the sample is affected, leading to the decrease in the degradation rate of MO at 5 min. Therefore, the optimal dosage of coal is 35%. All the MEF used in subsequent experiments were prepared under these conditions.

3.3 Optimization of Reaction Parameters of MEF

The degradation rate of MO by MEF was evaluated by varying the dosage of MEF in Fig. 5.

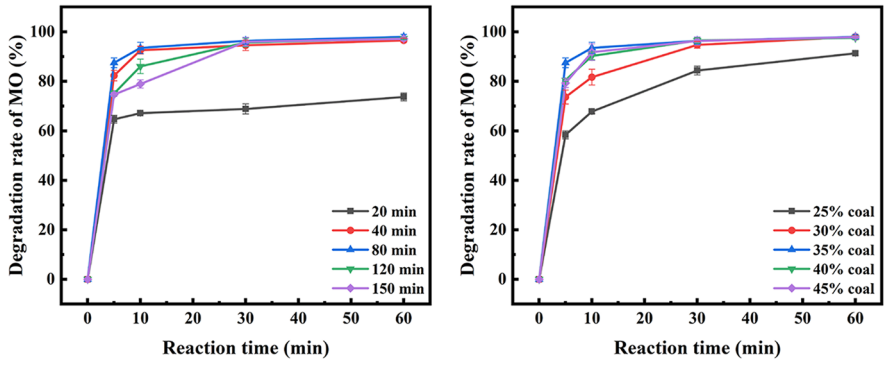

Fig. 4 Effects of **a** roasting time and **b** coal dosage on the degradation rate of MO

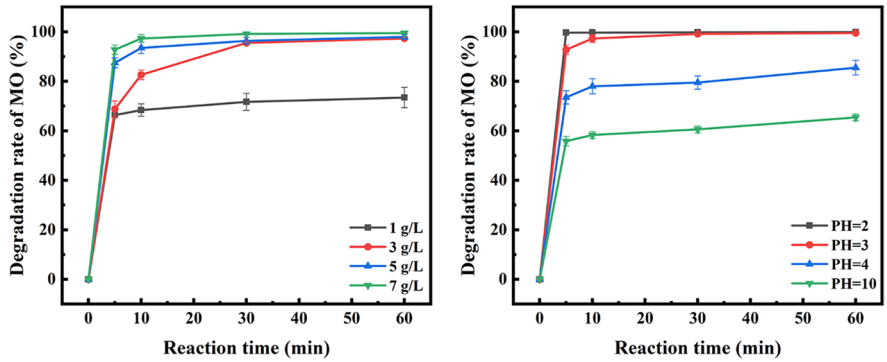

Fig. 5 Effects of **a** MEF dosage and **b** initial PH on the degradation rate of MO

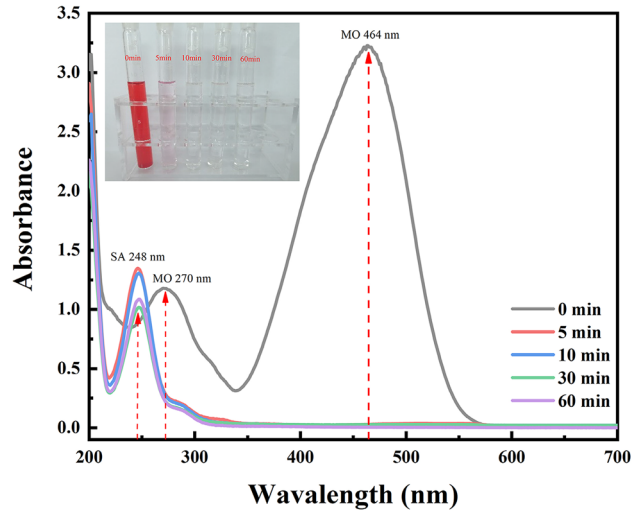

Fig. 6 Variation of UV–vis spectra of the MO aqueous solution during degradation process by MEF (7 g/L MEF dosage, solution pH 2)

As shown in Fig. 5 a, when the dosages of MEF are 1, 3, 5, and 7 g/L, the degradation rate rates of MO reach 66.36%, 68.81%, 87.49%, and 92.80% in 5 min, respectively. When the dosage of MEF is 7 g/L, the degradation rate of MO reaches 97.29% after 10 min of reaction, which is much higher than that of the three other parallel comparison groups. Increasing the amount of MEF will improve the active site of the reaction and thus accelerate the degradation rate. Therefore, the optimal dosage of MEF is 7 g/L.

The degradation rate of MO by MEF was evaluated by changing the initial pH value of the solution. As shown in Fig. 5 b, the degradation rate rates of MO at pH = 2, pH = 3, pH = 4, and pH = 10 at 5 min are 99.66%, 92.80%, 73.52%, and 55.82%, respectively.

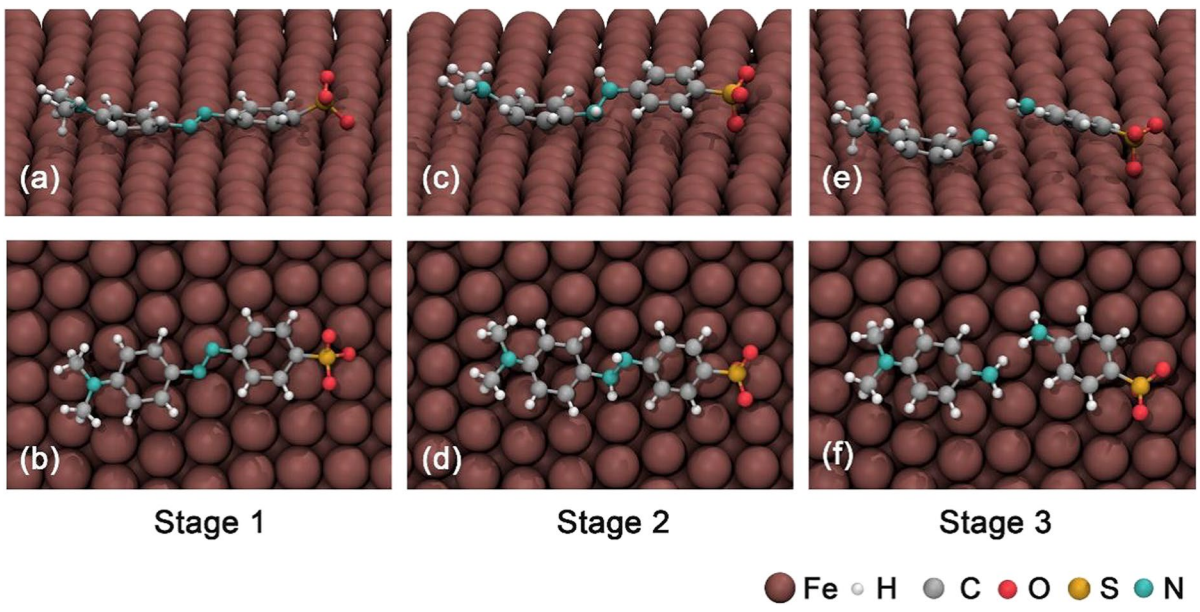

Fig. 7 The most stable configuration of the adsorption and dissociation on Fe (100) surface. **a**, **b** The side view and top view of the MO molecularly adsorbed on the Fe (100) surface, respectively; **c**, **d** the most stable configuration of the MO adsorption after bonding with two H^+; **e**, **f** the most stable structure of the dissociative adsorption of the MO on Fe (100) surface

With the decrease of initial pH, MEF significantly increases the degradation rate of pollutants, because more hydrogen ions are provided to the reaction system, resulting in an increase in the production of active hydrogen, which leads to the rapid destruction of the carbon chain of organic matter, consistent with the previous studies (Zhou et al., 2013a, b). The possible reasons for this phenomenon are as follows: Fe^0 is easily oxidized into Fe^{2+} under acidic conditions, promoting the occurrence of the reaction and generating a large amount of active hydrogen [H], which accelerates the destruction of the pollutant carbon chain. When the pH is high, hydroxide precipitates form covering the surface of ZVI and hindering the reaction (Yu et al., 2019a, b). Therefore, degradation of MO is not conducive under high pH conditions. Hence, the optimal initial pH value of the solution is 2.

3.4 Mechanism Analysis and DFT Study

3.4.1 UV–vis Spectral Analysis

The absorption spectrum of MO during the degradation process was recorded using UV spectroscopy. The solution was diluted twice before measurement, and the results are shown in Fig. 6.

The absorption spectrum of MO during the degradation process was recorded using UV spectroscopy. The solution was diluted twice before measurement, and the results are shown in Fig. 6. The characteristic absorption peak at 464 nm is caused by the electron transition ($\pi \rightarrow \pi^*$) resulting from the energy absorbed by the MO azo double bond (—N = N—). The characteristic absorption peak at 270 nm is caused by the aromatic ring (Chen et al., 2011; Lu et al., 2020).

During the degradation process, the peaks at 464 and 270 nm significantly reduce, and the color of the solution becomes lighter, indicating that the destruction of azo double bond of MO during degradation. Simultaneously, a new peak appears at 248 nm, likely due to the intermediate SA produced in the degradation process (Fan et al., 2009). The characteristic peak at 248 nm decreases with the increase of reaction time, implying the degradation of the generated intermediate substance during the reaction process. When the reaction reaches 60 min, the peak at 248 nm is higher than that at 30 min. This phenomenon may be due to the presence of a large number of hydrogen ions in the solution consumed or precipitates being formed and covering the surface of iron in the later stages of the reaction leading to the reduction in the degradation rate of MEF. At this point, the amount of the generated SA generated is greater than the amount of the degraded SA.

3.4.2 DFT Calculation Results

Figure 7 shows the most stable configuration of the adsorption and dissociation of MO on the Fe (100) surface. For stage 1, as shown in Fig. 7 a and b, an MO molecule is adsorbed on the Fe surface, and the molecule is parallel to the surface. One of the S–O bond binds to the Fe surface. The distances between the O atom in

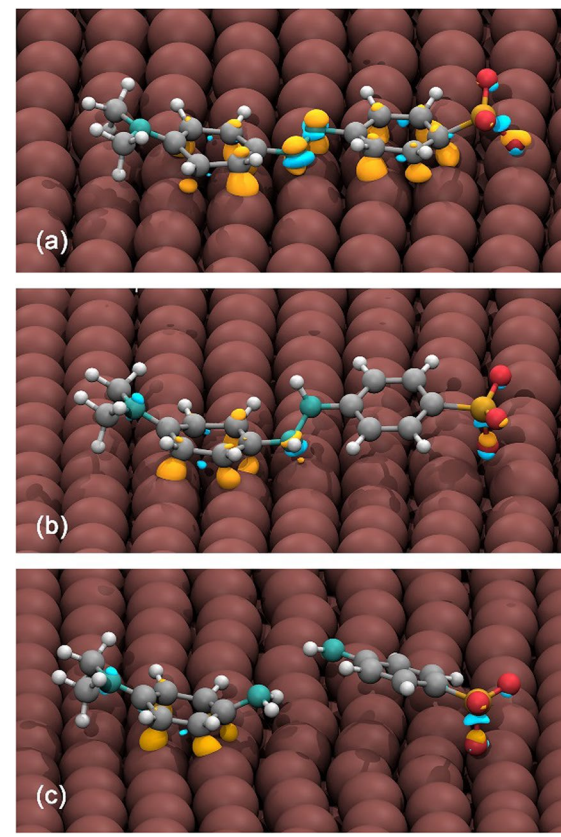

Fig. 8 Charge density difference of the MO adsorption on Fe (100) surface. **a** Stage 1; **b** stage 2; **c** stage 3. The color code of atoms corresponds to Fig. 5. The iso-value is set to 0.001 e-/Bohr3.The yellow and blue region represent charge accumulation and the charge depletion, respectively

MO and its two closest Fe atoms are 2.24 and 2.29 Å, respectively, which are close to the Fe–O bond length in iron oxides such Fe_2O_3. This phenomenon indicates the formation of Fe–O bond during the adsorption process. Moving to stage 2, two H^+ are adsorbed on the N atoms of the MO, which leads to a slight molecular reconstruction. One of the N atoms is away from the Fe (100) surface, while the overall adsorption configuration of the molecule insignificantly changes. Figure 7 e and f show the dissociation adsorption configuration of MO on the Fe (100) surface. The MO molecule with two H atoms dissociates into N,N-dimethyl-p-phenylenediamine and 4-aminobenzenesulfonate. Both molecules are adsorbed in parallel on the Fe (100) surface, with 4-aminobenzenesulfonate being farther from the surface, which indicating a higher possibility of desorption.

To further investigate the chemical interaction between MO and the Fe (100) surface, the charge density difference (CDD) was calculated by Eq. 7 as follows:

$$\Delta\rho = \rho_{AB} - \rho_A - \rho_B \tag{7}$$

where ρ_{AB}, ρ_A, and ρ_B represent the charge density of the MO + Fe slab, MO molecule, and Fe (100) surface slab, respectively. The CDD maps of the three adsorption stages are illustrated in Fig. 8. For pristine MO (Fig. 8a), its adsorption is primarily governed by the π-bond interactions between the two benzene rings and the Fe surface. The two N atoms also engage in electronic interactions with surface Fe atoms. However, with the addition of hydrogen ions (Fig. 8b), one of the benzene rings moves away from the surface, and the adsorption of the MO molecule relies on one benzene ring and one N atom. Moving to stage 3, the dissociated N,N-dimethyl-p-phenylenediamine molecule mainly interacts with the Fe surface through the π-bond of its benzene ring, while the dissociated 4-aminobenzenesulfonate molecule mainly forms bonds with the Fe surface through its O atom in the SO_3 functional group.

Figure 9 shows the electron density of states of C–Fe and O–Fe atom pairs in stage 3. The Fe–O bond is mainly contributed by the orbital overlap of the O-2 s, O-2p, and Fe-4d orbitals. The C–Fe bond is mainly formed by the orbital overlap of the C-2p and Fe-4d orbitals. These overlapping electronic orbitals confirm the chemical reaction between MO and the Fe (100) surface in the adsorption process.

4 Conclusion

Nickel slag can serve as an iron source for the preparation of MEF. The batch test showed that the amount of coal and roasting time significantly affected the

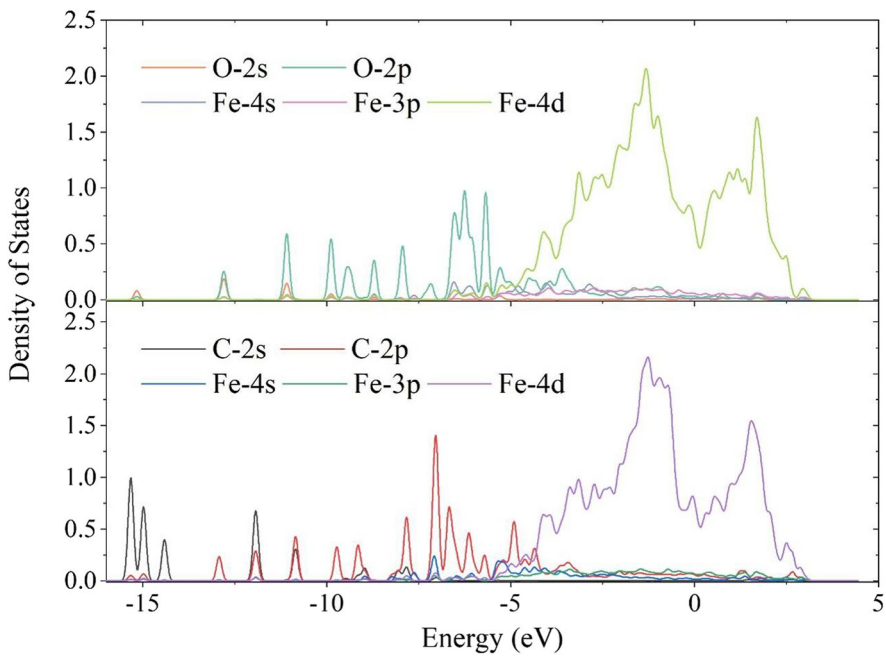

Fig. 9 The electron density of states of O–Fe and C–Fe atom pairs

degradation of MO by MEF. Meanwhile, increasing the amount of MEF and adjusting the pH could greatly improve the degradation efficiency of MO. The optimum process and reaction conditions were as follows: coal dosage of 35%, roasting time of 80 min, MEF dosage of 7 g/L, and initial pH of the solution set to 2. Under the optimal conditions, the degradation rate of MO reached 99.66% within 5 min.

The result of XRD and SEM–EDS showed the NS could be prepared MEF at 1200 °C. It is believed that cause of MO degradation corroding the UV spectrogram was due to the redox reactions between the active hydrogen [H] generated by MEF and MO, resulting in the destruction of the azo double bond of MO and the formation of SA.

DFT simulations reveal that during the adsorption process, the MO molecules form Fe–O bonds with the Fe surface and interact with the Fe surface through π-bond interactions. The chemical reaction process between the MO molecules and the Fe (100) surface was further confirmed by electronic density of states analysis.

Funding This study was funded by the State Key Laboratory of Complex Nonferrous Metal Resources Clean Utilization, Kunming University of Science and Technology under Grant No. CNMRCUKF2006, Open Foundation of State Key Laboratory of Mineral Processing under Grant No. BGRIMM-KJSKL-2020–25, and Foundation of Zhejiang Provincial Natural Science Foundation of China under Grant No. LQ21E040002.

Data Availability The data that support the findings of this study are available from the corresponding author upon reasonable request.

References

Arsalan, S., & Sarrafzadeh, M.-H. (2018). Effect of nitrifiers community on fouling mitigation and nitrification efficiency in a membrane bioreactor. *Chemical Engineering & Processing: Process Intensification, 128*, 10–18.

Arsalan, S., & Sarrafzadeh, M.-H. (2019). Activity enhancement of ammonia-oxidizing bacteria and nitrite-oxidizing bacteria in activated sludge process: Metabolite reduction and CO2 mitigation intensification process. *Applied Water Science, 9*, 131.

Arsalan, S., Sarrafzadeh M-H, Avateffazeli M. (2020). Interaction between *Chlorella vulgaris* and nitrifying-enriched activated sludge in the treatment of wastewater with low C/N ratio. *Journal of Cleaner Production, 247*, 119164.

Chen, Z. X., Jin, X. Y., Chen, Z. L., Megharaj, M., & Naidu, R. (2011). Removal of methyl orange from aqueous solution using bentonite-supported nanoscale zero-valent iron. *Journal of Colloid and Interface Science, 363*, 601–607.

Dai, F., Fan, X. R., Stratton, G. R., Bellona, C. L., Holsen, T. M., Crimmins, B. S., Xia, X. Y., & Mededovic Thagard, S. (2016). Experimental and density functional theoretical study of the effects of Fenton's reaction on the degradation of Bisphenol A in a high voltage plasma reactor. *Journal of Hazardous Materials, 308*, 419–429.

Emad, E., & Chaudhuri, M. (2009). Optimization of Fenton process for treatment of amoxicillin, ampicillin and cloxacillin antibiotics in aqueous solution. *Journal of Hazardous Materials, 170*, 666–672.

Fan, J., Guo, Y. F., Wang, J. J., & Fan, M. H. (2009). Rapid decolorization of azo dye methyl orange in aqueous solution by nanoscale zerovalent iron particles. *Journal of Hazardous Materials, 166*, 904–910.

Ge, X., Yu, S. S., Cheng, R. F., Chen, W. X., Zhou, F. Y., Liang, K., Chen, J. J., Yu, H. Q., & Wu, Y. E. (2021). Controllable drilling by corrosive Cu_1O_x to access highly accessible single-site catalysts for bacterial disinfection. *Applied Catalysis B: Environmental, 293*, 120228.

Ge, X., Xie, D. H., Cheng, R. F., Chen, W. X., Chen, C., Zhou, F. Y., Wang, X. Z., Chen, J. J., Sheng, G. P., & Wu, Y. E. (2023). Three-dimensional welded Mn1 site catalysts with nearly 100% Singlet oxygen fabrication for contaminant elimination. *Precision Chemistry, 1*, 153–160.

Ge, X., Zhou, D. Q., Wang, J., Yin, W. Q., Wang, X. Z., & Wu, Y. E. (2024). Rational regulation of the electronic structure of Cu_1 sites catalyst to modulate persulphate activation pathway. *Chemical Engineering Journal, 481*, 148587.

Gomathi Devi, L., Girish Kumar, S., Mohan Reddy, K., & Munikrishnappa, C. (2009). Photo degradation of methyl orange an azo dye by advanced Fenton process using zero valent metallic iron: Influence of various reaction parameters and its degradation mechanism. *Journal of Hazardous Materials, 164*, 459–467.

Grimme, S. (2006). Semiempirical GGA-type density functional constructed with a long-range dispersion correction. *Journal of Computational Chemistry, 27*, 1787–1799.

Hammer, B., Hansen, L. B., & Norskov, J. K. (1999). Improved adsorption energetics within density-functional theory using revised Perdew-Burke-Ernzerhof functionals. *Physical Review B, 59*, 7413–7421.

Li, X. B., Xiao, W., Liu, W., Liu, G. H., Peng, Z. H., Zhou, Q. S., & Qi, T. G. (2009). Recovery of alumina and ferric oxide from Bayer red mud rich in iron by reduction sintering. *Transactions of Nonferrous Metals Society of China, 19*, 1342–1347.

Liu, W. J., Jia, Z. X., Liu, Z. Y., Hu, W. P., Wang, X. T., & Dang, Y. F. (2018). How does palladium–amino acid cooperative catalysis enable regio- and stereoselective $C(sp^3)$–H functionalization in aldehydes and ketones? *A DFT Mechanistic Study, ACS Catalysis, 8*, 7698–7709.

Lu, C. L., Sun, W., Yue, T., Han, H. S., Yu, W., Nguyen, A. V., & Wang, L. (2020). A way out of the alkaline bauxite

residue: Synthesizing micro-electrolysis composite material towards the synergistic fenton degradation of high-concentration organic wastewater. *Journal of Hazardous Materials, 400*, 123210.

Ma, B., Zhang, H. H., Huang, T. L., Chen, S. L., Sun, W. M., Yang, W. Q., Niu, L. M., Liu, X., Liu, H. Y., Pan, S. X., Liu, H., & Zhang, X. L. (2023). Aerobic denitrification enhanced by immobilized slow-released iron/activated carbon aquagel treatment of low C/N micropolluted water: Denitrification performance, denitrifying bacterial community co-occurrence, and Implications. *Environmental Science & Technology, 57*, 5252–5263.

Maragkos, I., Giannopoulou, I. P., & Panias, D. (2009). Synthesis of ferronickel slag-based geopolymers. *Minerals Engineering, 22*, 196–203.

Monkhorst, H. J., & Pack, J. D. (1976). Special points for Brillouin-zone integrations. *Physical Review B, 13*, 5188–5192.

Peng, Z. W., Gu, F. Q., Zhang, Y. B., Tang, H. M., Ye, L., Tian, W. G., Liang, G. S., Rao, M. J., Li, G. H., & Jiang, T. (2018). Chromium: A double-edged sword in preparation of refractory materials from ferronickel slag. *ACS Sustainable Chemistry & Engineering, 6*, 10536–10544.

Sood, S., Mehta, S. K., Sinha, A. S. K., & Kansal, S. K. (2016). Bi_2O_3/TiO_2 heterostructures: Synthesis, characterization and their application in solar light mediated photocatalyzed degradation of an antibiotic, ofloxacin. *Chemical Engineering Journal, 290*, 45–52.

Sun, L., Wang, C., Ji, M., & Kong, X. (2013). Treatment of mixed chemical wastewater and the agglomeration mechanism via an internal electrolysis filter. *Chemical Engineering Journal, 215–216*, 50–56.

Sun, J., Wei, B., Mei, Q., An, Z. X., Wang, X. Y., Han, D. D., Xie, J., Zhan, J. H., Zhang, Q. Z., Wang, W. X., & He, M. X. (2020). Theoretical investigation on the degradation of dibutyl phthalate initiated by OH and $SO_4^{\cdot-}$ in aqueous solution: Mechanism, kinetics and ecotoxicity assessment. *Chemical Engineering Journal, 382*, 122791.

Sun, Z. G., Li, J. C., Yang, X. C., & Wang, M. T. (2023). Investigation on high-magnesium nickel slag treated by phase-separated activation as cementitious material. *Journal of Building Engineering, 69*, 106265.

Wang, M. H., Zhao, H., Liu, Y., Kong, C. Y., Yang, A. M., & Li, J. Y. (2017a). Removal of Fe from fly ash by carbon thermal reduction. *Microporous and Mesoporous Materials, 245*, 133–137.

Wang, S. S., Gao, B., Li, Y. C., Creamer, A. E., & He, F. (2017b). Adsorptive removal of arsenate from aqueous solutions by biochar supported zero-valent iron nanocomposite: Batch and continuous flow tests. *Journal of Hazardous Materials, 322*, 172–181.

Wang, Y., Wu, X. W., Yi, J., Chen, L. J., Lan, T. X., & Dai, J. (2018). Pretreatment of printing and dyeing wastewater by Fe/C micro-electrolysis combined with H_2O_2 process. *Water Science and Technology, 2017*, 707–717.

Wu, Q. S., Jiang, M., & Zhang, W. J. (2022). Preparation of adsorbent from nickel slag for removal of phosphorus from glyphosate by-product salt. *Separation Science and Technology, 57*, 2393–2406.

Yang, S. Y., Wang, P., Yang, X., Shan, L., Zhang, W. Y., Shao, X. T., & Niu, R. (2010). Degradation efficiencies of azo dye Acid Orange 7 by the interaction of heat, UV and anions with common oxidants: Persulfate, peroxymonosulfate and hydrogen peroxide. *Journal of Hazardous Materials, 179*, 552–558.

Yu, W., Tang, Q. Y., Chen, J. A., & Sun, T. C. (2016). Thermodynamic analysis of the carbothermic reduction of a high-phosphorus oolitic iron ore by FactSage. *International Journal of Minerals, Metallurgy, and Materials, 23*, 1126–1132.

Yu, D. Y., Cui, J., Wang, Y., & Pei, Y. S. (2019a). Removal of ibuprofen by using a novel Fe/C granule-induced heterogeneous persulfate system at near neutral pH. *Industrial & Engineering Chemistry Research, 59*, 1073–1082.

Yu, W., Sun, Y. Y., Lei, M. J., Chen, S. M., Qiu, T. S., & Tang, Q. Y. (2019b). Preparation of micro-electrolysis material from flotation waste of copper slag and its application for degradation of organic contaminants in water. *Journal of Hazardous Materials, 361*, 221–227.

Zaharaki, D., & Komnitsas, K. (2009). Effect of additives on the compressive strength of slag-based inorganic polymers. *Global Nest Journal, 11*, 137–146.

Zhang, Q. Z., Qu, X. H., & Wang, W. X. (2007). Mechanism of OH-Initiated atmospheric photooxidation of dichlorvos: A quantum mechanical study. *Environmental Science & Technology, 41*, 6109–6116.

Zhang, Q. Z., Gao, R., Xu, F., Zhou, Q., Jiang, G. B., Wang, T., Chen, J. M., Hu, J. T., Jiang, W., & Wang, W. X. (2014). Role of water molecule in the gas-phase formation process of nitrated polycyclic aromatic hydrocarbons in the atmosphere: A computational study. *Environmental Science & Technology, 48*, 5051–5057.

Zhou, H. M., Lv, P., Shen, Y. Y., Wang, J. J., & Fan, J. (2013a). Identification of degradation products of ionic liquids in an ultrasound assisted zero-valent iron activated carbon micro-electrolysis system and their degradation mechanism. *Water Research, 47*, 3514–3522.

Zhou, H. M., Shen, Y. Y., Lv, P., Wang, J. J., & Fan, J. (2013b). Degradation of 1-butyl-3-methylimidazolium chloride ionic liquid by ultrasound and zero-valent iron/activated carbon. *Separation and Purification Technology, 104*, 208–213.

Zhu, Q. S., Guo, S. H., Guo, C. M., Dai, D., Jiao, X. K., Ma, T. Q., & Chen, J. F. (2014). Stability of Fe–C microelectrolysis and biological process in treating ultra-high concentration organic wastewater. *Chemical Engineering Journal, 255*, 535–540.